



# Analysis of Voltage Losses in PEM Water Electrolyzers with Low Platinum Group Metal Loadings

Maximilian Bernt,<sup>1,2,\*<sup>z</sup></sup> Armin Siebel,<sup>1,2,\*</sup> and Hubert A. Gasteiger<sup>2,\*\*</sup>

<sup>1</sup>Bayerisches Zentrum für angewandte Energieforschung, 85748 Garching, Germany

<sup>2</sup>Chair of Technical Electrochemistry, Department of Chemistry and Catalysis Research Center, Technical University of Munich, 85748 Garching, Germany

In this study, the influence of catalyst loading on the performance of a proton exchange membrane (PEM) water electrolyzer is investigated (Nafion 212 membrane; IrO<sub>2</sub>/TiO<sub>2</sub> (anode) and Pt/C (cathode)). Due to the fast kinetics of the hydrogen evolution reaction (HER) on platinum (Pt), the Pt loading on the cathode can be reduced from 0.30 mg<sub>Pt</sub> cm<sup>-2</sup> to 0.025 mg<sub>Pt</sub> cm<sup>-2</sup> without any negative effect on performance. On the anode, the iridium (Ir) loading was varied between 0.20–5.41 mg<sub>Ir</sub> cm<sup>-2</sup> and an optimum in performance at operational current densities ( $\geq 1$  A cm<sup>-2</sup>) was found for 1–2 mg<sub>Ir</sub> cm<sup>-2</sup>. At higher Ir loadings, the performance decreases at high current densities due to insufficient water transport through the catalyst layer whereas at Ir loadings  $< 0.5$  mg<sub>Ir</sub> cm<sup>-2</sup> the catalyst layer becomes inhomogeneous, which leads to a lower electrochemically active area and catalyst utilization, resulting in a significant decrease of performance. To investigate the potential for a large-scale application of PEM water electrolysis, the Ir-specific power density (g<sub>Ir</sub> kW<sup>-1</sup>) for membrane electrode assemblies (MEAs) with different catalyst loadings is analyzed as a function of voltage efficiency, and the consequences regarding catalyst material requirements are discussed.

© The Author(s) 2018. Published by ECS. This is an open access article distributed under the terms of the Creative Commons Attribution 4.0 License (CC BY, <http://creativecommons.org/licenses/by/4.0/>), which permits unrestricted reuse of the work in any medium, provided the original work is properly cited. [DOI: [10.1149/2.0641805jes](https://doi.org/10.1149/2.0641805jes)]



Manuscript submitted January 22, 2018; revised manuscript received March 15, 2018. Published March 28, 2018. This was Paper 1382 presented at the New Orleans, Louisiana, Meeting of the Society, May 28–June 1, 2017.

PEM water electrolysis could provide electrolytic hydrogen for large-scale energy storage and mobility in a future energy scenario based on renewable energy sources. Currently, only a small share of the global hydrogen demand is served by PEM electrolysis due to the relatively high costs associated with this technology.<sup>1,2</sup> Overall H<sub>2</sub> costs are influenced by operating costs, which are governed by electricity prices and the efficiency of the electrolyzer, as well as system costs. According to a 2014 report by the EU's FCHJU, 70–90% of the projected long-term costs for H<sub>2</sub> production via PEM water electrolysis are due to the cost of electricity, so that significant improvements of the overall H<sub>2</sub> production efficiency are desired, proposing a 2030 target of 64–76%<sub>LHV</sub> (based on the lower heating value of hydrogen, LHV).<sup>1</sup> For currently installed systems (size typically in the kW–to MW–range),<sup>1–3</sup> the contribution of catalyst costs to the total system costs are comparably small ( $\approx 5\%$ ).<sup>1,4,5</sup> Consequently, high platinum group metal (PGM) loadings (several mg<sub>PGM</sub> cm<sup>-2</sup>), namely mostly platinum (Pt) to catalyze the hydrogen evolution reaction (HER) and iridium (Ir) to catalyze the oxygen evolution reaction (OER), are used to ensure good performance and lifetime.<sup>6</sup> However, as the PEM electrolyzer stack power is being increased to the MW-scale, the contribution of balance-of-plant costs is predicted to be much lower, and catalyst costs will become a major cost contributor.<sup>3</sup>

An equally important consideration for the envisaged large-scale application of PEM water electrolyzers in renewable energy generation/storage are the supply constraints for Ir and Pt.<sup>1</sup> While the fast HER kinetics of Pt<sup>7,8</sup> at the hydrogen cathode suggest that a reduction of the Pt loading would not significantly affect the electrolyzer performance, this is not the case for the oxygen anode, owing to the much slower OER kinetics on iridium oxide surfaces. Hence, a growing concern in the context of large-scale PEM water electrolysis applications is the availability of Ir, which is one of the rarest materials on earth with an estimated annual production of only  $\approx 4$  tons.<sup>4</sup> In a recent study by Babic et al., the authors estimate that if 25% of the annually produced Ir were to be used for PEM water electrolysis and considering that current PEM water electrolyzers require  $\approx 0.5$  g<sub>Ir</sub> kW<sup>-1</sup>, the annual PEM water electrolyzer installation would be limited to 2 GW/year.<sup>4</sup>

This currently estimated maximum Ir-supply limited annual PEM water electrolyzer installation capacity may be compared to the water

electrolysis capacity which would be needed, for example, if a large fraction of the currently used fossil fuels in the transportation sector were to be replaced by hydrogen. The worldwide fossil energy demand for transportation is currently 10<sup>20</sup> Joule<sup>9</sup> and, assuming that this demand would have to be supplied by H<sub>2</sub>, this would equal to an annual production of 700 Mt<sub>H2</sub> (based on the H<sub>2</sub> higher heating value (HHV) of 285.8 kJ/mol). At the above mentioned long-term electrolyzer efficiency of  $\approx 70$  %<sub>LHV</sub> (corresponding to a cell voltage of  $\approx 1.79$  V), this corresponds to an average electric power of  $\approx 3800$  GW. Taking into account that electrolyzers would be coupled to fluctuating renewable energy sources and could not run permanently at full load, the required world-wide installed electrolyzer power would be approximately three-fold higher, i.e.,  $\approx 12000$  GW (assuming, e.g., an average production power of roughly one third of its peak power available from wind farms).<sup>1</sup> From this example, it becomes clear that an installed capacity on the order of  $\approx 150$  GW/year would be necessary to completely decarbonize the mobility sector by the end of this century. Even when assuming that 50% of the Ir production could be used for PEM water electrolysis, this would require a  $\approx 50$ -fold reduction of today's Ir-specific power density down to  $\approx 0.01$  g<sub>Ir</sub> kW<sup>-1</sup> while maintaining a high efficiency. Whether this is feasible based on the OER activity of current Ir-based catalyst will be the focus of this study.

In general, it is possible to reduce the Ir-specific power density by reducing the catalyst loading as well as by increasing the current density. However, both will result in an increase of cell voltage and, consequently, a lower efficiency. Therefore, the final catalyst loading as well as the operating point (i.e., the current density) will be dictated by Ir price and availability.<sup>10</sup> Different approaches to reduce Ir loadings are reported in the literature, e.g., maximizing the noble metal dispersion by supporting thin films or nanoparticles of iridium (oxide) on high surface area support materials like TiC,<sup>11</sup> TaC,<sup>12</sup> TiO<sub>2</sub>,<sup>13</sup> or nano-structured thin films (NSTF),<sup>14</sup> whereby for the latter it was shown that high performance is possible even at Ir loadings  $< 0.5$  mg<sub>Ir</sub> cm<sup>-2</sup>.<sup>14</sup> Fabrication of core-shell catalysts and usage of improved catalyst layer manufacturing techniques like reactive spray deposition have also been proposed as pathways to achieve low Ir loadings.<sup>3</sup> However, most catalysts used in these studies are experimental materials and not yet commercially available. Additionally, there are only few studies which systematically analyze the effect of Ir loading on the performance and the voltage losses of an electrolyzer,<sup>15,16</sup> suggesting that loadings as low as 0.1 mg<sub>Ir</sub> cm<sup>-2</sup> can deliver high performance and durability.

\*Electrochemical Society Student Member.

\*\*Electrochemical Society Fellow.

<sup>z</sup>E-mail: [maximilian.bernt@tum.de](mailto:maximilian.bernt@tum.de)

In this study, we present a detailed investigation of the influence of widely ranging cathode and anode catalyst loadings on electrolyzer performance for in-house prepared MEAs with typical commercial catalyst materials, viz., carbon-supported platinum (Pt/C) and IrO<sub>2</sub>-coated titanium (IrO<sub>2</sub>/TiO<sub>2</sub>). We identify the optimum in performance depending on current density and analyze the occurring voltage losses. Furthermore, we address the question whether it is possible to reach the above outlined target values for the Ir-specific power density ( $\approx 0.01 \text{ g}_{\text{Ir}} \text{ kW}^{-1}$ ) with today's state-of-the-art catalysts.

## Experimental

**Membrane electrode assembly (MEA) preparation and cell assembly.**—5 cm<sup>2</sup> MEAs were prepared by a decal transfer method. Platinum supported on Vulcan XC72 carbon with two different metal loadings (45.8 wt% Pt/C, TEC10V50E and 4.8 wt% Pt/C, TEC10V05E from Tanaka, Kikinzoku Kogyo, Japan) was used as catalyst for the hydrogen evolution reaction at the cathode. For the oxygen evolution anode, IrO<sub>2</sub> supported on TiO<sub>2</sub> (IrO<sub>2</sub>/TiO<sub>2</sub> with 75 wt% iridium; Elyst Ir75 0480 from Umicore, Germany) was used. Suspensions were prepared by mixing catalyst powder, a solvent (either 2-propanol, purity  $\geq 99.9\%$  or acetone, purity  $\geq 99.9\%$ , from Sigma Aldrich, Germany), de-ionized (DI) water (18 MΩ cm) and Nafion ionomer solution (1100 EW, 20 wt% ionomer; D2021 from IonPower, USA) for 24 hours using a roller mill (rotating at 180 rpm). To achieve a homogenous suspension, ZrO<sub>2</sub> grinding beads (5 mm diameter) were added to 2–5 ml of the ink dispersion contained in a 8 ml polypropylene bottle.

The resulting catalyst ink was then coated onto a thin plastic foil (25 μm thick ETFE (FP361025 from Goodfellow, UK) or 50 μm thick PTFE (from Angst+Pfister, Germany)) using a Mayer-rod coating machine. After drying, electrodes with an active area of 5 cm<sup>2</sup> were punched from the coatings and hot-pressed onto a Nafion 212 membrane (50 μm thick; from Quintech, Germany) for 3 min at 155°C at a pressure of 2.5 MPa. The catalyst loading was determined by weighing the ETFE/PTFE decals before and after the decal transfer step, using a microbalance ( $\pm 15 \mu\text{g}$ ; Mettler Toledo XPE105DR). For the cathode electrodes with an ionomer to carbon weight ratio of 0.6/1, the loadings were  $0.30 \pm 0.05 \text{ mg}_{\text{Pt}} \text{ cm}_{\text{MEA}}^{-2}$  (45.8 wt% Pt/C) and  $0.025 \pm 0.007 \text{ mg}_{\text{Pt}} \text{ cm}_{\text{MEA}}^{-2}$  (4.8 wt% Pt/C), respectively; the electrode thicknesses, calculated from the average packing density of the resulting Vulcan carbon supported catalyst layers ( $22 \pm 4 \mu\text{m} (\text{mg}_{\text{Vulcan}} \text{ cm}^{-2})^{-1}$ ),<sup>17</sup> were very similar, viz.,  $\approx 8 \mu\text{m}$  for the high-loaded and  $\approx 11 \mu\text{m}$  for the low-loaded cathode. For the anode, the solid content of the inks as well as the wet-film thickness of the coatings was varied to obtain catalyst loadings between 0.20–5.41 mg<sub>Ir</sub> cm<sub>MEA</sub><sup>-2</sup>, while the ionomer content was kept at 11.6 wt% relative to the total weight of the electrode (shown to yield the optimum performance in our earlier study).<sup>18</sup>

Sintered titanium (from Mott Corporation, USA) with a porosity of  $\approx 50\%$  and a thickness of  $280 \pm 10 \mu\text{m}$  as well as a carbon fiber paper (TGP-H-120T without MPL, 20 wt% PTFE; from Toray, Japan) with a thickness of  $370 \pm 10 \mu\text{m}$  were used as porous transport layers (PTL) at the anode and at the cathode, respectively. The MEA and PTLs were placed between the flow fields of the electrolyzer test cell and sealed with virgin PTFE gaskets. Sealings with an appropriate thickness were chosen to achieve  $\approx 25\%$  compression of the carbon PTL (under the applied compression, the titanium PTL is considered incompressible). Details of the cell hardware and the cell assembly are described elsewhere.<sup>18</sup>

**Physical characterization.**—Cross-sectional scanning electron microscopy (SEM) samples were prepared by embedding MEAs (after electrochemical characterization) in room-temperature curing epoxy. The sample surface was ground with SiC paper in two steps (grade P320 and P1200, from Buehler, Germany) and subsequently polished with 9 μm diamond polishing agent. SEM analysis was performed with a JEOL JSM-7500F scanning electron microscope at an accelerating voltage of 5–15 kV. The electrode thickness was measured

at 10–15 different locations of an MEA cross-section to account for local inhomogeneity of the electrode thickness.

**Electrochemical characterization.**—An automated test station from Greenlight Innovation, equipped with a potentiostat and booster (Reference 3000 and 30 A booster, Gamry), was used for electrochemical characterization of the MEAs. The cell temperature was fixed to 80°C and deionized (DI) water was pre-heated to 80°C and fed to anode and cathode of the electrolysis cell at a rate of 5 ml min<sup>-1</sup>. Polarization curves were recorded at pressures ranging from 1–30 bar absolute pressure (bar<sub>a</sub>). The product gas at the anode outlet was diluted with nitrogen (200 nccm) to prevent the formation of an explosive gas mixture, which can be produced by the permeation of H<sub>2</sub> through the membrane into the anode compartment, especially at high pressure and low current densities.

After a warm-up step under N<sub>2</sub> atmosphere, the cell was conditioned at 1 A cm<sup>-2</sup> for 30 min. Subsequently, galvanostatic polarization curves were recorded in a current range from 0.01 to 6 A cm<sup>-2</sup>. At each current, the cell voltage was averaged over 10 s after 5 min equilibration time. The first two polarization curves were considered part of the conditioning process and were thus not included in the data analysis. Galvanostatic AC impedance measurements between 100 kHz – 1 Hz were carried out after each polarization step. The amplitude of the current perturbation was chosen for each step to obtain a sufficient signal to noise ratio, while keeping the perturbation small enough to ensure a linear system response. The high-frequency resistance (HFR) was obtained from the high-frequency intercept of the Nyquist plot with the real axis. All polarization curves and corresponding HFR values reported in this work represent an average of three consecutive measurements for a single MEA. The standard deviation of the three measurements was evaluated and included as error bars in all figures (note that for most samples the standard deviation is too small to be visible in the graphs).

Cyclic voltammograms (CVs) of the IrO<sub>2</sub>/TiO<sub>2</sub> anode electrode were recorded at the beginning of a test, using a scan rate of 50 mV s<sup>-1</sup> at 80°C. The anode working electrode was flushed with H<sub>2</sub>O at a flow rate of 5 ml min<sup>-1</sup>, while the cathode counter electrode was purged with dry H<sub>2</sub> at 50 ml min<sup>-1</sup>. Except for the CV test, it was ensured that the cell potential did not drop below  $\approx 1.3$  V during the entire test in order to prevent a reduction of the IrO<sub>2</sub> on the anode, as this was shown to lead to a change in activity and Tafel slope.<sup>19</sup>

## Results and Discussion

**Platinum loading in cathode catalyst layer.**—To study the influence of the Pt loading on the cathode, two MEAs with Pt loadings of  $0.30 \text{ mg}_{\text{Pt}} \text{ cm}^{-2}$  (red curve in Fig. 1) and  $0.025 \text{ mg}_{\text{Pt}} \text{ cm}^{-2}$  (blue curve in Fig. 1) were tested. The different loadings were obtained by using Pt/C catalysts with Pt metal loadings of 45.8 wt% and 4.8 wt% while keeping the electrode thickness of both samples similar ( $\approx 8 \mu\text{m}$  for the high loaded and  $\approx 11 \mu\text{m}$  for the low loaded cathode). For these experiments, the Ir loading on the anode was kept constant for both MEAs ( $\approx 1.6 \text{ mg}_{\text{Ir}} \text{ cm}^{-2}$ ). Polarization curves including the measured cell voltage,  $E_{\text{cell}}$ , as well as the iR-free cell voltage,  $E_{\text{iR-free}}$ , are shown in Fig. 1, together with the corresponding HFR values. Obviously, the cell voltage is very similar for both MEAs (cf. Fig. 1a). The slightly higher cell voltage at high current densities for the MEA with low Pt loading (amounting to  $\approx 20$  mV at 6 A cm<sup>-2</sup>) may be partially due to its higher overpotential for the HER and proton transport resistance in the catalyst layer, but may also partially be caused by the slightly higher HFR obtained for this cell (58 vs. 53 mΩ cm<sup>2</sup>, Fig. 1b), resulting in the observation that the iR-free cell voltage (dashed line in Fig. 1a) is almost identical for both MEAs, i.e., for both high and low cathode loadings. Tafel slopes – obtained from a linear fit of the iR-free cell voltage for current densities between 10–100 mA cm<sup>-2</sup> – are also identical within the experimental error for both samples (47–48 mV dec<sup>-1</sup>, cf. inset in Fig. 1a).

The expected overpotentials for HER kinetics and cathode proton transport can be calculated as shown in our previous work<sup>18</sup> (cf.

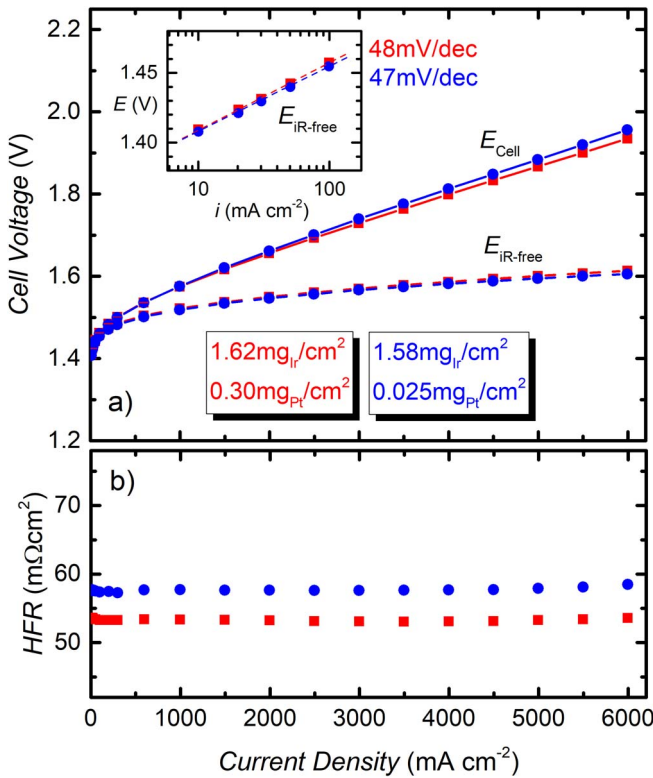


**Figure 1.** a) Ambient pressure polarization curves ( $80^\circ\text{C}$ ,  $5 \text{ ml}_{\text{H}_2\text{O}} \text{ min}^{-1}$ ) of MEAs with different cathode catalyst loadings (red:  $0.30 \text{ mg}_{\text{Pt}} \text{ cm}^{-2}$  with 45.8 wt% Pt/C; blue:  $0.025 \text{ mg}_{\text{Pt}} \text{ cm}^{-2}$  with 4.8 wt% Pt/C) and with standard anode Ir loadings ( $\approx 1.6 \text{ mg}_{\text{Ir}} \text{ cm}^{-2}$ ) using a  $\approx 50 \mu\text{m}$  thick Nafion 212 membrane. The full lines represent the measured cell voltage, the dashed lines give the cell voltage corrected by the HFR. The inset shows a Tafel plot of the iR-free cell voltages, with the Tafel slope values obtained from a linear fit between  $10\text{--}100 \text{ mA cm}^{-2}$ . b) HFR-values vs. current density obtained by electrochemical impedance spectroscopy.

Appendix for detailed calculation) and result in an overall difference of  $\approx 7.5 \text{ m}\Omega \text{ cm}^2$  between high-loaded and low-loaded cathode. This would amount to a cell voltage difference of  $\approx 45 \text{ mV}$  at  $6 \text{ A cm}^{-2}$  (assuming a similar HFR for both MEAs), which is close to the observed value ( $\approx 20 \text{ mV}$  at  $6 \text{ A cm}^{-2}$ ). The HFR difference of  $\approx 5 \text{ m}\Omega \text{ cm}^2$  between high-loaded and low-loaded cathodes is observed systematically for all tested samples. Here it should be mentioned, however, that the difference in the measured HFR values ( $\approx 10\%$ ) is close to within our estimated experimental accuracy for this measurement. Furthermore, we cannot exclude that the HFR values obtained from the x-axis intercept in a Nyquist plot are affected by the different HER overpotentials for high-loaded and low-loaded cathodes, i.e. that the different HER semi-circles (which occur at rather high frequencies) in the Nyquist plot distort the determination of the HFR. However, since the expected difference for HER kinetics and proton transport ( $\approx 7.5 \text{ m}\Omega \text{ cm}^2$ ) is on the same order as the observed HFR difference ( $\approx 5 \text{ m}\Omega \text{ cm}^2$ ) between the two MEAs, we cannot reliably deconvolute these differences, but can clearly state that ultra-low cathode Pt loadings produce minor performance differences (on the order of 10 mV) within typical operating current densities ( $< 3 \text{ A cm}^{-2}$ ).

Consequently, we can consider the beginning-of-life performance of a PEM water electrolyzer operated at  $80^\circ\text{C}$  as essentially independent of the cathode Pt loading down to  $\approx 0.025 \text{ mg}_{\text{Pt}} \text{ cm}^{-2}$ . By extension, this implies that the apparent Tafel slope determined from the inset in Fig. 1a corresponds to the Tafel slope for the OER on the  $\text{IrO}_2/\text{TiO}_2$  catalyst, in agreement with the value determined in our earlier publication.<sup>18</sup> Catalyst degradation during prolonged operation could, of course, be more severe for lower cathode loadings and

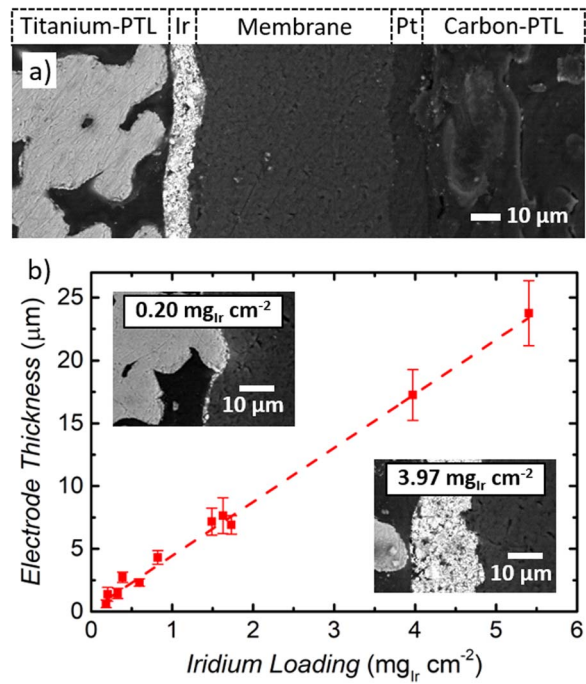


**Figure 2.** a) Cross-sectional SEM image of an MEA with an Ir loading of  $1.58 \text{ mg}_{\text{Ir}} \text{ cm}^{-2}$  and Pt loading of  $0.025 \text{ mg}_{\text{Pt}} \text{ cm}^{-2}$ . From left to right: anode PTL (titanium sinter), anode electrode composed of  $\text{IrO}_2/\text{TiO}_2$  catalyst and ionomer,  $50 \mu\text{m}$  thick Nafion 212 membrane, cathode electrode composed of 4.8 wt% Pt/C and ionomer, cathode PTL (carbon paper). b) Electrode thickness determined from 10–15 individual measurements on cross-sectional SEM images vs. iridium loading determined from the areal weight of the anode electrodes; the dashed line is a linear regression line of anode thickness ( $t_{\text{anode}}$ ) vs. iridium loading ( $L_{\text{Ir}}$ ), yielding  $t_{\text{anode}} = 4.3 \pm 0.3 \mu\text{m} (\text{mg}_{\text{Ir}} \text{ cm}^{-2})^{-1} \cdot L_{\text{Ir}}$ . The insets show SEM images of an MEA with a low Ir loading ( $0.20 \text{ mg}_{\text{Ir}} \text{ cm}^{-2}$ , electrode thickness  $\approx 1 \mu\text{m}$ ) and a high Ir loading ( $3.97 \text{ mg}_{\text{Ir}} \text{ cm}^{-2}$ ,  $\approx 17 \mu\text{m}$ ).

hence, the influence of catalyst loading on the long-term performance requires further investigation. In our example, the final Pt loading of  $0.025 \text{ mg}_{\text{Pt}} \text{ cm}^{-2}$  is almost two orders of magnitude lower than the standard Ir loading of  $\approx 1.6 \text{ mg}_{\text{Ir}} \text{ cm}^{-2}$ , indicating that the main challenges toward a substantial reduction of noble metal loading remain at the anode of the electrolyzer. Consequently, the rest of our study will focus on the influence of the Ir anode loading on PEM electrolyzer performance.

**Iridium loading in anode catalyst layer.**—The commercial state-of-the-art catalyst for the anode used in this study has a fixed Ir metal content of 75 wt% and hence, adjusting the iridium loading in the range of  $0.20\text{--}5.41 \text{ mg}_{\text{Ir}} \text{ cm}^{-2}$  was accompanied by a variation of the anode electrode thickness. Thus, for each MEA, cross-sectional SEM micrographs were recorded (cf. Fig. 2a, where it is exemplarily shown for an MEA with the standard Ir loading of  $\approx 1.6 \text{ mg}_{\text{Ir}} \text{ cm}^{-2}$ ), from which the electrode thickness as a function of Ir loading was determined (cf. Fig. 2b). As one would expect, the anode thickness scales linearly with the catalyst loading (from  $\approx 1\text{--}25 \mu\text{m}$ ), corresponding to an effective packing density of  $4.3 \pm 0.3 \mu\text{m} (\text{mg}_{\text{Ir}} \text{ cm}^{-2})^{-1}$  (cf. Fig. 2b). Error bars represent the standard deviation for 10–15 measurements on each electrode. The insets in Fig. 2b exemplarily show the SEM images of two extreme Ir loadings ( $0.20 \text{ mg}_{\text{Ir}} \text{ cm}^{-2}$  vs.  $3.97 \text{ mg}_{\text{Ir}} \text{ cm}^{-2}$ ), which will be relevant to the further analysis below.

Polarization curves at ambient pressure and  $80^\circ\text{C}$  were recorded for all MEAs. In order to facilitate the direct comparison of the performance at various Ir loadings, the iR-free cell voltage,  $E_{\text{iR-free}}$ , at three current densities is displayed as a function of Ir loading in Fig. 3. Here,  $E_{\text{iR-free}}$  is defined as the cell voltage,  $E_{\text{cell}}$ , corrected by the measured HFR, which represents the sum of the membrane resistance,

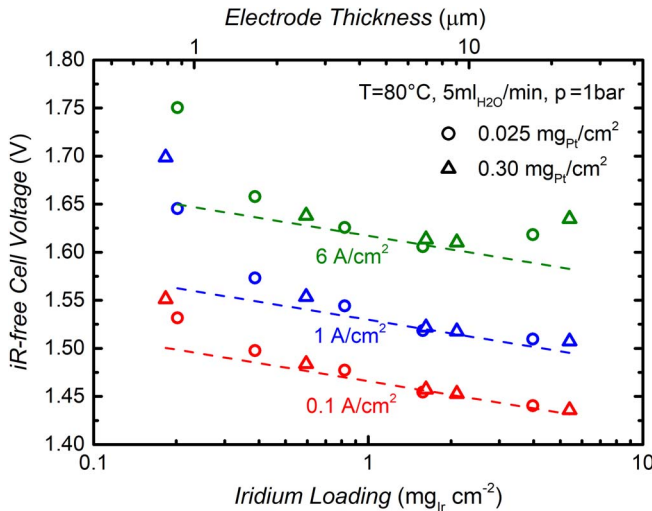


**Figure 3.** Ambient pressure cell voltage corrected by HFR,  $E_{iR\text{-free}}$ , at current densities of  $0.1 \text{ A cm}^{-2}$ ,  $1.0 \text{ A cm}^{-2}$  and  $6.0 \text{ A cm}^{-2}$  ( $80^\circ\text{C}$ ,  $5 \text{ mL}_\text{H}_2\text{O}/\text{min}$ ,  $p = 1 \text{ bar}$ ) as a function of anode iridium loading. The dashed lines represent the expected  $iR$ -free cell voltage based on the performance of the MEAs with standard Ir loadings ( $\approx 1.6 \text{ mg}_{\text{Ir}} \text{ cm}^2 \text{ MEA}^{-2}$ ), assuming that only the OER overpotential changes with Ir loading (Tafel slope:  $\approx 47 \text{ mV dec}^{-1}$ ). MEAs with low Pt loadings ( $\approx 0.025 \text{ mg}_{\text{Pt}} \text{ cm}^2 \text{ MEA}^{-2}$ ) are represented by circles, MEAs with high Pt loadings ( $\approx 0.30 \text{ mg}_{\text{Pt}} \text{ cm}^2 \text{ MEA}^{-2}$ ) are shown by triangles.

$R_{\text{memb}}$ , and the electronic resistance,  $R_{\text{el}}$ :

$$\begin{aligned} E_{iR\text{-free}} &\equiv E_{\text{cell}} - i \cdot (R_{\text{memb}} + R_{\text{el}}) \\ &= E_{\text{rev}} + \eta_{\text{HER}} + \eta_{\text{OER}} + i \cdot (R_{\text{H}^+,\text{an}}^{\text{eff}} + R_{\text{H}^+,\text{cath}}^{\text{eff}}) + \eta_{\text{mt}} \quad [1] \end{aligned}$$

The right-hand-side of Eq. 1 shows the reversible cell voltage,  $E_{\text{rev}}$ , to which all other voltage loss terms are added (note that current, potentials, and overpotentials are taken as positive values here): i)  $\eta_{\text{HER}}$  and  $\eta_{\text{OER}}$  are the kinetic overpotentials for the HER and the OER; ii)  $R_{\text{H}^+,\text{an}}^{\text{eff}}$  and  $R_{\text{H}^+,\text{cath}}^{\text{eff}}$  represent the effective proton transport resistance in anode and cathode catalyst layer, respectively; and iii)  $\eta_{\text{mt}}$  represents any residual mass transport resistance(s) (for examples see Reference 18).

For the smallest current density ( $0.1 \text{ A cm}^{-2}$ ; red symbols), mass transport  $\eta_{\text{mt}}$  and proton transport ( $R_{\text{H}^+,\text{an}}^{\text{eff}} + R_{\text{H}^+,\text{cath}}^{\text{eff}}$ ) can be considered negligible, so that the  $iR$ -free potential shown in Fig. 3 should be exclusively governed by the OER kinetics (HER kinetics can be neglected as discussed in the previous section). In this case, at constant  $\text{H}_2/\text{O}_2$  partial pressures and temperature, and under the assumption that the OER can be described by simple Tafel kinetics, one would expect that  $E_{iR\text{-free}}$  should be described by:

$$E_{iR\text{-free}} \propto TS \cdot \log(i) - TS \cdot \log(i_{0(\text{OER})} \cdot A_{\text{Ir},\text{el}} \cdot L_{\text{Ir}}) \quad [2]$$

where  $TS$  is the Tafel slope for the OER,  $i_{0(\text{OER})}$  is the OER exchange current density,  $A_{\text{Ir},\text{el}}$  is the specific surface area of the anode catalyst, and  $L_{\text{Ir}}$  is the iridium catalyst loading. Thus, when using the same anode catalyst (i.e.,  $A_{\text{Ir},\text{el}} = \text{constant}$ ) and for constant current density, Eq. 2 yields:

$$\left( \frac{\partial E_{iR\text{-free}}}{\partial \log L_{\text{Ir}}} \right)_{A_{\text{Ir},\text{el}}, i, T, p_{\text{O}_2}, p_{\text{H}_2}} = -TS \quad [3]$$

With an intrinsic OER Tafel slope of  $TS \approx 47 \text{ mV dec}^{-1}$  (see inset in Fig. 1a), at a low and constant current density, a plot of  $E_{iR\text{-free}}$  vs. the logarithm of the iridium loading of each MEA should follow a straight line with a slope of  $47 \text{ mV dec}^{-1}$ . This expected trend for  $E_{iR\text{-free}}$  vs.  $\log(L_{\text{Ir}})$  at  $0.1 \text{ A cm}^{-2}$  is indicated by the dashed red line in Fig. 3, demonstrating that the measured data points follow the prediction very well, down to a catalyst loading of  $\approx 0.5 \text{ mg}_{\text{Ir}} \text{ cm}^{-2}$ . However, for lower Ir loadings,  $E_{iR\text{-free}}$  is higher than expected for an OER kinetics controlled regime, indicating additional voltage loss

contributions even at such low current density, the origin of which will be discussed in the next Section.

In general, Eqs. 2 and 3 are not expected to be valid at a current density of  $1 \text{ A cm}^{-2}$ , where transport related resistances, particularly related to proton conduction in the anode and  $\text{H}_2$  mass transport resistances in the cathode, become appreciable (amounting to a total of  $\approx 20 \text{ mV}$ , as shown in our previous work).<sup>18</sup> However, if these resistances were to be independent of the Ir loading (as expected, e.g., for resistances caused by the  $\text{H}_2$  cathode), one would still expect the same  $47 \text{ mV dec}^{-1}$  slope of  $E_{iR\text{-free}}$  vs.  $\log(L_{\text{Ir}})$  at  $1 \text{ A cm}^{-2}$ , but offset from the  $0.1 \text{ A cm}^{-2}$  line by a bit more than  $47 \text{ mV}$ . However, except for a narrow range of Ir loadings ( $\approx 0.8\text{--}2.0 \text{ mg}_{\text{Ir}} \text{ cm}^{-2}$ ), this is not the case (see blue symbols in Fig. 3). Most noteworthy, as the Ir loading and thus the anode catalyst layer thickness decreases, the magnitude of additional transport related losses increases ( $>100 \text{ mV}$  at the lowest loading of  $0.2 \text{ mg}_{\text{Ir}} \text{ cm}^{-2}$ ), even though one would expect rather the opposite, as thinner electrodes would have lower ( $i \cdot R_{\text{H}^+,\text{an}}^{\text{eff}}$ ) losses.

At the highest current density of  $6 \text{ A cm}^{-2}$  (green symbols in Fig. 3), the presence of additional resistances at low Ir loadings is also apparent, but now pronounced transport related losses can also be observed at high Ir loadings (at  $\approx 4$  and  $5.4 \text{ mg}_{\text{Ir}} \text{ cm}^{-2}$ ), suggesting a different anode loading (or thickness) dependent transport resistance. Based on the analysis in Fig. 3, transport related voltage losses are minimized and optimal cell performance is obtained for Ir loadings in the range of  $\approx 1\text{--}2 \text{ mg}_{\text{Ir}} \text{ cm}^{-2}$  with anode electrode thicknesses of  $\approx 4\text{--}8 \mu\text{m}$ . It should be mentioned at this point, that some of the MEAs shown in Fig. 3 have cathode electrodes with a high Pt loading (triangles), while others have low Pt loadings (circles). As expected from our earlier analysis of different Pt loadings (see the previous section), the Pt loading does not influence the performance. The effects leading to an increase of cell voltage at very low and high Ir loadings, associated with very thin and very thick electrodes, are discussed in more detail in the following sections.

**High iridium loadings.**—The polarization curve of an MEA with a high Ir loading ( $3.97 \text{ mg}_{\text{Ir}} \text{ cm}^{-2}$ ; brown lines/symbols) is compared to a standard MEA in Fig. 4a ( $1.58 \text{ mg}_{\text{Ir}} \text{ cm}^{-2}$ ; blue lines/symbols). At low current densities, i.e., in the kinetic region,  $E_{iR\text{-free}}$  is slightly lower for the sample with a high Ir loading (cf. inset in Fig. 4a). This is expected due to the higher electrochemically active surface area compared to the standard Ir loading. An estimation based on a simple Tafel equation (cf. Eq. 3) predicts a difference of  $\approx 19 \text{ mV}$ , which is very close to the experimentally observed value ( $\approx 15 \text{ mV}$ , cf. dashed red line in Fig. 3). At high current densities, on the other hand, the cell voltage of an MEA with high Ir loading is higher than for the standard MEA. This indicates additional voltage losses due to mass- and/or proton transport, which are expected to become more prominent in a  $\approx 2.5$ -fold thicker electrode ( $\approx 7 \text{ vs. } \approx 17 \mu\text{m}$ , cf. Fig. 2). The effective proton transport resistance,  $R_{\text{H}^+,\text{an}}^{\text{eff}}$ , and the corresponding voltage loss can be estimated as shown in more detail in a previous study.<sup>18</sup> From this calculation, one would expect an additional penalty of  $\approx 15 \text{ mV}$  at  $6 \text{ A cm}^{-2}$  for the MEA with a high Ir loading ( $3.97 \text{ mg}_{\text{Ir}} \text{ cm}^{-2}$ ) compared to the standard MEA ( $1.58 \text{ mg}_{\text{Ir}} \text{ cm}^{-2}$ ). This, however, can only partly explain the difference between measured and expected  $iR$ -free cell voltage considering the difference in OER overpotential ( $\approx 31 \text{ mV}$ , cf. green symbols and dashed line in Fig. 3), which indicates that a different additional mass transport resistance must be involved.

Insights into this phenomenon can be gained by examining the HFR, particularly its strong increase with current density for the high-loaded/thick anode electrode (cf. Fig. 4b). This is in stark contrast to the standard MEA with a lower anode loading and a thinner anode electrode, for which the HFR is essentially independent of current density. Moreover, if there were a dependency of the HFR on current density, one would expect the HFR to rather decrease with increasing current density, as a concomitant increase in heat production could result in a local temperature increase at the electrode/membrane interface, leading to a higher ionic conductivity of the membrane.<sup>20</sup>

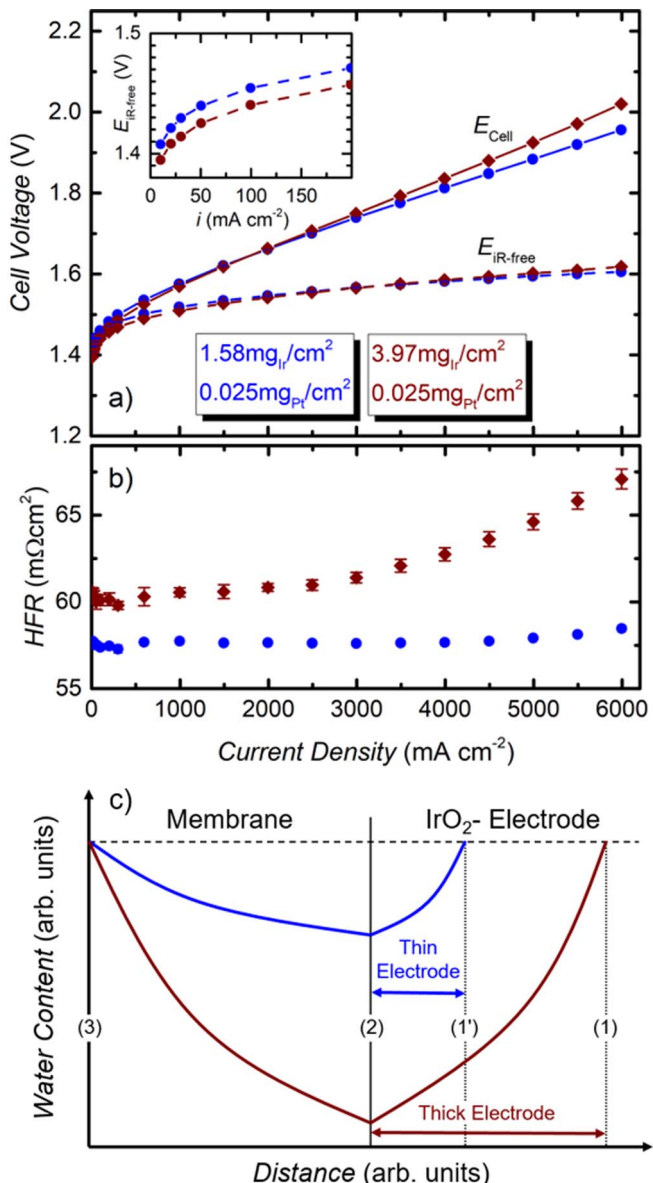


**Figure 4.** a) Ambient pressure polarization curves ( $80^{\circ}\text{C}$ ,  $5 \text{ mlH}_2\text{O min}^{-1}$ ) for an MEA with a high Ir loading ( $3.97 \text{ mg}_{\text{Ir}} \text{ cm}_{\text{MEA}}^{-2}$ , with a thickness of  $\approx 17 \mu\text{m}$ ) compared to the MEA with standard loading ( $1.58 \text{ mg}_{\text{Ir}} \text{ cm}_{\text{MEA}}^{-2}$ , with a thickness of  $\approx 7 \mu\text{m}$ ), both using a  $\approx 50 \mu\text{m}$  thick Nafion 212 membrane and  $0.025 \text{ mg}_{\text{Pt}} \text{ cm}_{\text{MEA}}^{-2}$  cathodes. The full lines represent the measured cell voltage, the dashed lines give the cell voltage corrected by HFR ( $E_{\text{iR-free}}$ ). The inset shows a magnification of the iR-free cell voltage at small current densities. b) Corresponding HFR values. c) Qualitative sketch of the water concentration profile within the membrane and the anode catalyst layer for the two anode electrodes with different thicknesses, marking: (1) anode/PTL interface for the thick anode electrode, (1') anode/PTL interface for the thin anode electrode, (2) membrane/anode electrode interface, and, (3) cathode electrode/membrane interface.

Nevertheless, in this case it would also be expected for the low-loaded anode. As the HFR represents the sum of electronic contact resistance and membrane resistance, either of these factors could be responsible for the observed HFR increase with current density. However, since the contact resistance should be independent of the applied current, the only logical explanation is that this effect is related to the membrane resistance. A similar increase of the HFR for high current densities was previously observed for PEM fuel cells when comparably thick membranes ( $\geq 50 \mu\text{m}$ ) were used.<sup>21,22</sup> Springer et al. showed that this HFR increase is related to a change of the water profile across the

membrane when increasing the current density,<sup>21</sup> owing to the electroosmotic water drag rate from anode to cathode which is roughly proportional to the current density: at high current densities, the water flux due to electroosmotic drag is too high to be compensated by back diffusion of water from cathode to anode, resulting in a lower water content in the anode-near region of the membrane and, consequently, an increase of the HFR.<sup>21</sup>

Based on these findings, we propose a similar model for our electrolyzer MEA to explain the increase of HFR with current density for thick (high-loaded) anode electrodes. A qualitative water profile across the membrane and anode catalyst layer is illustrated in Fig. 4c for a thin and a thick anode electrode, respectively. In the case of an electrolyzer, excess liquid water is supplied to the anode, so that we can always assume an equally high water content at the anode/PTL interface ((1) and (1') in Fig. 4c), independent of current density. The amount of water transported to the membrane/anode interface ((2) in Fig. 4c) is then controlled by the thickness of the electrode, which acts as a diffusion barrier for water transport. In principle, liquid water transport across the anode electrode should be rather rapid within the free void volume of the electrode ( $\approx 35\%$  void volume fraction for the 11.6 wt% ionomer containing anode),<sup>18</sup> but with increasing current density, the void volume will likely be filled more and more by  $\text{O}_2$ , thereby gradually limiting water transport to the ionomer phase (its volume fraction is also  $\approx 35\%$ ).<sup>18</sup> Once the latter becomes dominating, the water transport resistance through the thick anode electrode ( $\approx 17 \mu\text{m}$ ) should of course be higher than for the thin electrode ( $\approx 7 \mu\text{m}$ ), and water transport toward the membrane is slower. At the same time, with increasing current density, the water transport from anode to cathode ((3) in Fig. 4c) due to electroosmotic drag (drag coefficient of 2.4–3.4)<sup>23,24</sup> increases and at some point cannot be compensated by the comparably slow water transport through the thick anode electrode anymore. This would lead to a lower water content in the anode-near region of the membrane and, consequently, an increase of the membrane resistance. This could very well explain why the HFR for the MEA with a high Ir loading ( $3.97 \text{ mg}_{\text{Ir}} \text{ cm}^{-2}$ ) starts to increase significantly for current densities above  $3 \text{ A cm}^{-2}$  while it is constant up to  $6 \text{ A cm}^{-2}$  for the MEA with standard Ir loading ( $1.58 \text{ mg}_{\text{Ir}} \text{ cm}^{-2}$ ).

Assuming this hypothesis to be correct, a decrease of the oxygen volume fraction within the anode electrode by increasing the oxygen pressure should either increase the current density above which an increase of the HFR is observed or even eliminate this effect. The latter is indeed observed in Fig. 5, comparing polarization curves for the MEA with an Ir loading of  $3.97 \text{ mg}_{\text{Ir}} \text{ cm}^{-2}$  at ambient pressure (brown lines/symbols) and balanced pressure ( $p_{\text{H}_2} = p_{\text{O}_2}$ ) of 30 bar<sub>a</sub> (green lines/symbols). Interestingly, at high pressure, the HFR does no longer increase with current density (Fig. 5b). Instead, even a slight decrease is observed at high current densities, as would be expected due to a local increase of temperature with current (see above). This shows that the increase of operating pressure on the anode improves the water transport through the anode electrode, preventing a decrease of the water content in the anode-near region of the membrane. This effect is clearly related to the higher anode pressure, because a similar behavior was not observed when only the cathode was pressurized (data not shown). Thus, at high operating pressure, a lower volume fraction of  $\text{O}_2$  gas in the pores of the catalyst layer and/or smaller  $\text{O}_2$  bubbles seem to be clearly beneficial for the transport of water.<sup>25,26</sup> However, the two-phase flow inside the catalyst layer is a very complex topic and more research is required to fully understand the phenomena.<sup>27</sup>

**Low iridium loadings.**—The polarization curve of an MEA with a low Ir loading ( $0.20 \text{ mg}_{\text{Ir}} \text{ cm}^{-2}$ , with  $\approx 1 \mu\text{m}$  thickness; orange lines/symbols) is shown in Fig. 6, again compared to a standard MEA ( $1.58 \text{ mg}_{\text{Ir}} \text{ cm}^{-2}$ , with  $\approx 7 \mu\text{m}$  thickness; blue lines/symbols). The cell voltage of the MEA with low Ir loading is significantly higher than for the standard MEA, which can be partly explained by an increase of the HFR (30–40%), compared to the standard MEA (cf. Fig. 6b). However, even for the HFR-corrected cell voltage there is a difference of  $\approx 150 \text{ mV}$  already at  $1 \text{ A cm}^{-2}$ , which is much higher than the

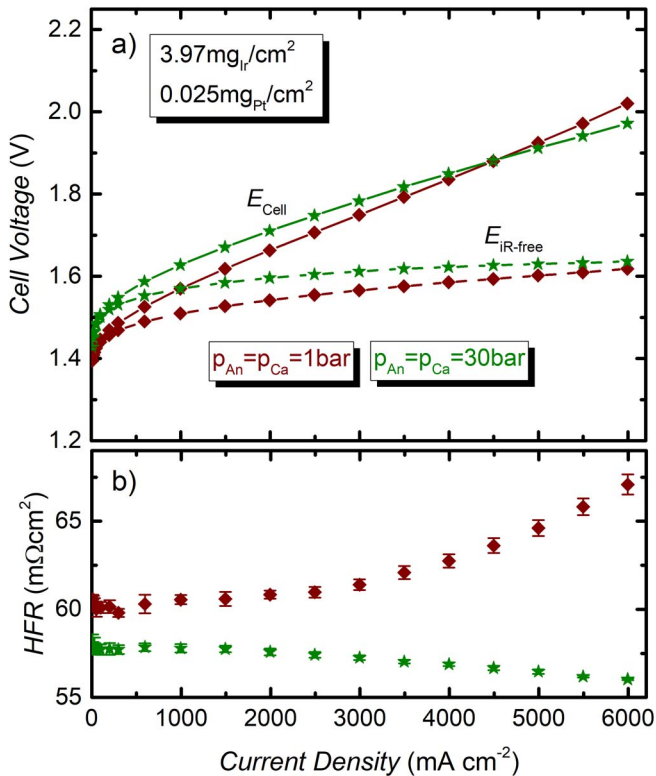


**Figure 5.** a) Polarization curves ( $80^\circ\text{C}$ ,  $5\text{ mlH}_2\text{O min}^{-1}$ ) for an MEA with a  $\approx 17\text{ }\mu\text{m}$  thick anode with an Ir loading of  $3.97\text{ mgIr cm}^{-2}$  (cathode:  $0.025\text{ mgPt cm}^{-2}$ ), operated at balanced pressures of 1 bar (brown) and 30 bar (green), respectively. The full lines represent the measured cell voltage, the dashed lines give the cell voltage corrected by HFR. b) Corresponding HFR.

expected increase of the kinetic OER overpotential of  $\approx 42\text{ mV}$  as calculated from Eq. 3. This clearly shows that additional voltage loss terms must be considered for MEAs with low-loaded and thin anodes.

In order to gain more insights into the behavior at low current densities, Tafel slopes were determined from a fit of the linear region between  $10\text{--}100\text{ mA cm}^{-2}$  (cf. Fig. 7). For the MEAs with standard Ir loading ( $1.58\text{ mgIr cm}^{-2}$ ) and high Ir loading ( $3.97\text{ mgIr cm}^{-2}$ ), the Tafel slopes are similar ( $47\text{ mV dec}^{-1}$  vs.  $45\text{ mV dec}^{-1}$ ) and the difference in  $E_{iR-free}$  at low current densities ( $\approx 15\text{ mV}$ ) is as expected from Eq. 3. At low Ir loading, on the other hand, there is a difference in  $E_{iR-free}$  of  $\approx 55\text{ mV}$  compared to the standard MEA, even at the lowest current density ( $0.01\text{ A cm}^{-2}$ ). This is higher than what would be expected from the OER kinetics ( $\approx 42\text{ mV}$ ), indicating additional voltage losses even at such low current densities. The difference in  $E_{iR-free}$  grows with increasing current density, which is also reflected by a significantly higher apparent Tafel slope of  $68\text{ mV dec}^{-1}$  for the MEA with the low Ir loading. Apart from a change of the OER reaction mechanism, which we consider utterly unlikely, since it is the same catalyst operating at almost the same potential, this discrepancy could point toward additional voltage losses even at very low current densities. Consequently, for the MEA with a  $\approx 1\text{ }\mu\text{m}$  thin low-loaded anode, the Tafel slope does no longer represent the pure OER kinetics in contrast to the MEAs with higher Ir loading. In fact, for Ir loadings  $> 1\text{ mgIr cm}^{-2}$ , all Tafel slopes are between  $45\text{--}50\text{ mV dec}^{-1}$  (cf. Fig. 7b), which is consistent with the results for an Ir loading of  $\approx 2\text{ mgIr cm}^{-2}$  from our previous study<sup>18</sup> as well as with literature values obtained with model electrodes.<sup>28,29</sup> For Ir loadings  $< 1\text{ mgIr cm}^{-2}$ , on the other hand, the apparent Tafel slope increases significantly.

The reasons for the additional voltage losses leading to an increase of the apparent Tafel slopes can be explained in terms of the electrode structure for low Ir loadings. Fig. 8a shows a cross-sectional SEM

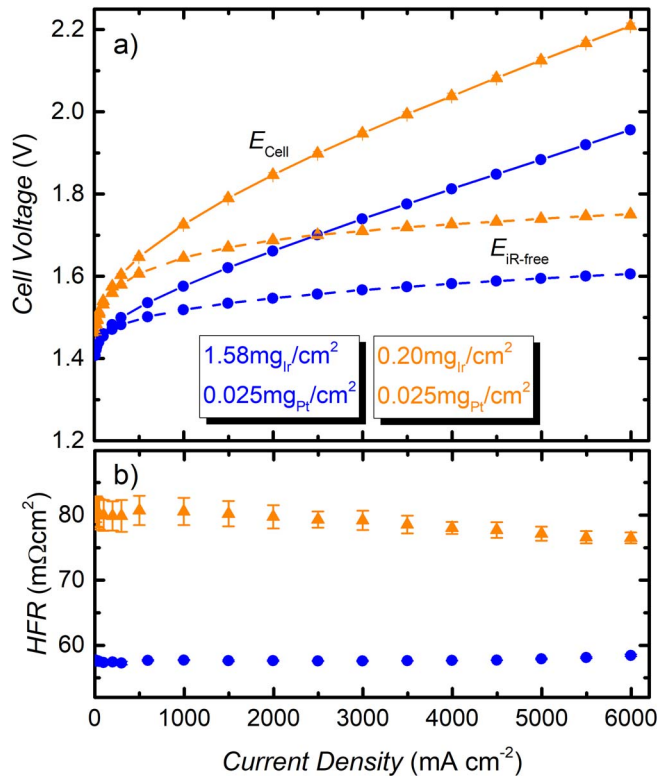


**Figure 6.** a) Ambient pressure polarization curves ( $80^\circ\text{C}$ ,  $5\text{ mlH}_2\text{O min}^{-1}$ ) for an MEA with a low Ir loading ( $0.20\text{ mgIr cm}^{-2}$ , with a thickness of  $\approx 1\text{ }\mu\text{m}$ ) compared to the MEA with standard loadings ( $1.58\text{ mgIr cm}^{-2}$ , with a thickness of  $\approx 7\text{ }\mu\text{m}$ ), both using a  $\approx 50\text{ }\mu\text{m}$  thick Nafion 212 membrane and a cathode loading of  $0.025\text{ mgPt cm}^{-2}$ . The full lines represent the measured cell voltage, the dashed lines give the cell voltage corrected by HFR. b) Corresponding HFR.

image of an anode electrode with a low Ir loading ( $0.20\text{ mgIr cm}^{-2}$ ). The nominal electrode thickness for this loading is only  $\approx 1\text{ }\mu\text{m}$ , leading to a non-uniform catalyst layer (cf. Fig. 8a). The reason for this inhomogeneity is related to the catalyst material itself which has typical structure sizes in the range of  $0.1\text{--}1\text{ }\mu\text{m}$  (cf. Fig. 8b). It is rather obvious that it is not possible to make a uniform  $\approx 1\text{ }\mu\text{m}$  thick catalyst layers when single catalyst particles are already on the same length scale. The result is an inhomogeneous catalyst layer, as evidenced by the top-view SEM image (Fig. 8b) of a  $0.20\text{ mgIr cm}^{-2}$  anode coated onto a Nafion membrane, where dark areas indicate  $\mu\text{m}$ -sized regions without any catalyst particles. However, since the free membrane patches in between the catalyst layer are of a dimension (on the order of  $0.5\text{--}2\text{ }\mu\text{m}$ ) which is more than an order of magnitude smaller than the thickness of the membrane, this cannot directly explain the higher HFR (see orange symbols in Fig. 6b).

Instead, we believe that the anomalously high HFR is related to the large pore sizes of the Ti PTL ( $10\text{--}50\text{ }\mu\text{m}$  pores) in combination with the low in-plane electronic conductivity of an inhomogeneous, non-contiguous anode catalyst layer, as outlined in the following. From Fig. 8a it becomes clear that due to the large structures of the PTL, not all parts of the catalyst layer are in direct electronic contact with the PTL, thus requiring in-plane electron conduction over distances of several tens of micrometers within the catalyst layer to enable the OER. For a thick and therefore contiguous catalyst layer (Fig. 8c), high in-plane electronic conductivity is provided by the good electronic conductivity of  $\text{IrO}_2$ . On the other hand, for a very thin and non-contiguous catalyst layer, the resistance for electron transport within the layer is expected to increase if electronic contact is not maintained throughout the entire catalyst layer, which in fact is evident from Fig. 8b. Therefore, segments of the low-loaded

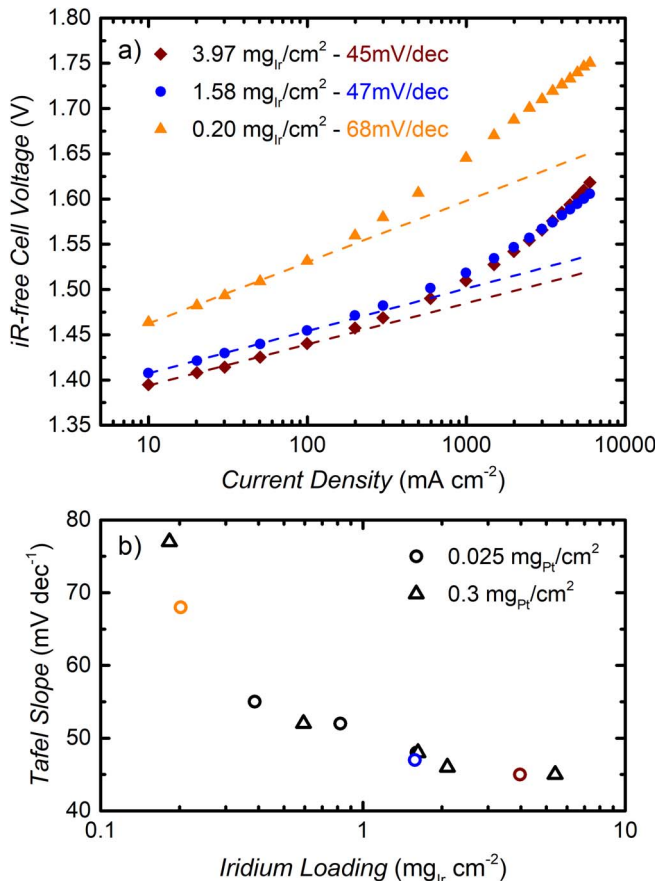


**Figure 7.** a) Ambient pressure Tafel plot of the  $iR$ -free cell voltage ( $80^\circ\text{C}$ ,  $5 \text{ mLH}_2\text{O min}^{-1}$ ) for different anode Ir loadings and thicknesses:  $0.20 \text{ mg}_{\text{Ir}} \text{ cm}_{\text{MEA}}^{-2}$  ( $\approx 1 \mu\text{m}$  thickness),  $1.58 \text{ mg}_{\text{Ir}} \text{ cm}_{\text{MEA}}^{-2}$  ( $\approx 7 \mu\text{m}$  thickness), and  $3.97 \text{ mg}_{\text{Ir}} \text{ cm}_{\text{MEA}}^{-2}$  ( $\approx 17 \mu\text{m}$  thickness). The Tafel slope is obtained from a linear fit of the values between  $10$ – $100 \text{ mA cm}^{-2}$ . b) Tafel slopes as a function of anode iridium loading. MEAs with low cathode loadings ( $\approx 0.025 \text{ mg}_{\text{Pt}} \text{ cm}_{\text{MEA}}^{-2}$ ) are represented by circles, MEAs with high cathode loadings ( $\approx 0.30 \text{ mg}_{\text{Pt}} \text{ cm}_{\text{MEA}}^{-2}$ ) are shown by triangles; the membrane was a  $\approx 50 \mu\text{m}$  thick Nafion 212.

anode catalyst layers with sizes comparable to the Ti PTL pore size ( $10$ – $50 \mu\text{m}$ ) will have poor or no electronic connection with the Ti PTL (see Fig. 8d), and will thus not participate in the OER. Furthermore, the fraction of inactive anode catalyst segments will increase with increasing current density (i.e., the catalyst utilization will decrease), resulting in the observed apparent increase of the Tafel slope. Under this hypothesis, the observed higher HFR for thin anodes (see orange symbols in Fig. 6b) is simply a consequence of the fact that the size of these electronically poorly connected patches are on the order of the thickness of the membrane.

This hypothesis can be probed by cyclic voltammetry (CV) as shown in our previous study,<sup>18</sup> where the mass normalized voltammetric charge,  $q^*$  (the sum of the absolute values of the anodic and cathodic charges), is used as a measure for the electrochemically active surface area.<sup>15,30,31</sup> Fig. 9a shows cyclic voltammograms of the anode electrode of the standard MEA with a  $\approx 7 \mu\text{m}$  thick anode (solid blue line) and the MEA with the  $\approx 1 \mu\text{m}$  thick low-loaded anode (dashed yellow line). Since the mass-specific current is plotted on the y-axis, one would expect similar voltammetric charges for both MEAs, independent of Ir loading. However,  $q^*$ , obtained by integration of the area under the CV, is  $\approx 35\%$  lower for the MEA with the low Ir loading, clearly showing a lower catalyst utilization for the thin, inhomogeneous and non-contiguous anode catalyst layer. Voltammetric charges,  $q^*$ , for all tested MEAs are shown in Fig. 9b. Here, it is readily observed that for Ir loadings  $< 0.5 \text{ mg}_{\text{Ir}} \text{ cm}^{-2}$ ,  $q^*$

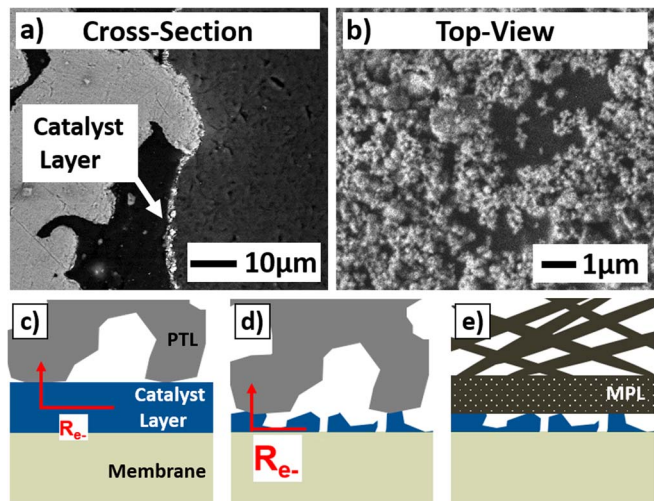


**Figure 8.** a) Cross-sectional SEM image of a  $\approx 1 \mu\text{m}$  thin anode catalyst layer with low Ir loading ( $0.20 \text{ mg}_{\text{Ir}} \text{ cm}_{\text{MEA}}^{-2}$ ). b) Top-view SEM image of the catalyst layer. Scheme illustrating the electronic transport within an anode catalyst layer and to the PTL for c) a homogeneous catalyst layer (Ir loading  $> 1 \text{ mg}_{\text{Ir}} \text{ cm}_{\text{MEA}}^{-2}$ ) and d) a thin, inhomogeneous catalyst layer (Ir loading  $< 0.50 \text{ mg}_{\text{Ir}} \text{ cm}_{\text{MEA}}^{-2}$ ). e) Replacement of Ti PTL by a carbon PTL with microporous layer (MPL) which has an effective pore size on the order of  $0.1 \mu\text{m}$ .

decreases significantly. As discussed before, we attribute this lower catalyst utilization to an insufficient in-plane electronic conductivity of the thin non-contiguous anode catalyst layer in combination with the large porous structure of the Ti PTL.

In order to prove this hypothesis, we replaced the Ti PTL with a carbon fiber paper, coated with a carbon-black based microporous layer (MPL) facing the anode catalyst layer, with the aim to improve the electronic contact with all segments of the anode electrode (cf. Fig. 8e). The pore size of the MPL is on the order of  $0.1 \mu\text{m}$ , and thus much smaller than that of the Ti PTL ( $10$ – $50 \mu\text{m}$ ). Using the carbon fiber paper with MPL, the CV of the MEA with low Ir loading (dotted purple line in Fig. 9a) now enlarges significantly, and its  $q^*$  value increases dramatically (see purple triangle in Fig. 9b) and reaches a value comparable to that of MEAs with Ir loadings  $> 1 \text{ mg}_{\text{Ir}} \text{ cm}^{-2}$ . This clearly supports our hypothesis that thin non-contiguous anode catalyst layers are characterized by a lower catalyst utilization, resulting from the combination of a large-pore PTL and an insufficient in-plane conductivity of the anode catalyst layer. It is important to note that this effect occurs already at very small absolute current densities during a CV measurement ( $\approx \pm 1.5 \text{ mA cm}^{-2}$  for the  $0.2 \text{ mg}_{\text{Ir}} \text{ cm}^{-2}$  anode shown in Fig. 9a). Since the in-plane electronic resistance within the catalyst layer will have a stronger effect at higher current densities (i.e., causing an even lower catalyst utilization), it is consistent with the observed disproportionately large increase of  $E_{iR\text{-free}}$  with current density for the MEA with low Ir loading (cf. Fig. 7a), the consequence of which is an apparently higher Tafel slope for MEAs with thin low-loaded anodes (cf. Fig. 7b). Ultimately, the application of a truly microporous MPL (pore size of  $< 1 \mu\text{m}$ ) could improve the performance of thin catalyst layers. Since the carbon paper would not be stable under OER conditions, a Ti PTL with MPL would be required and a beneficial effect of such a MPL has already been shown in the literature.<sup>32</sup>

**Iridium requirements for large-scale PEM electrolysis.**—Finally, we would like to discuss the implications of our analysis regarding the Ir requirements for a large-scale application of PEM electrolysis. As outlined in the Introduction section, there are several criteria which must be met: i) high cell voltage efficiency to minimize electricity cost (opex), with a 2030 target of  $\approx 70\%_{\text{LHV}}$  ( $\equiv 1.79 \text{ V}$  cell voltage); ii) high current densities to minimize the investment cost (capex); and

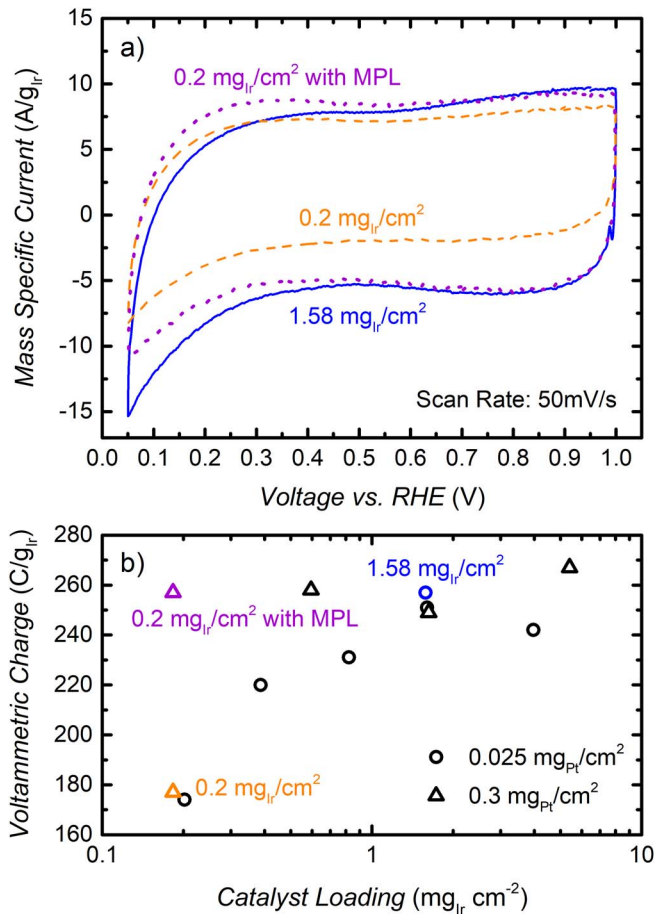


**Figure 9.** a) Ambient pressure cyclic voltammograms (CV) of  $\text{IrO}_2/\text{TiO}_2$  based anodes with different Ir loadings:  $0.2 \text{ mg}_{\text{Ir}} \text{ cm}^{-2}$  ( $\approx 1 \mu\text{m}$  thickness) and  $1.58 \text{ mg}_{\text{Ir}} \text{ cm}^{-2}$  ( $\approx 7 \mu\text{m}$  thickness). The mass-specific current is plotted vs. the applied potential. CVs were recorded at a scan rate of  $50 \text{ mV s}^{-1}$  at  $80^\circ\text{C}$ .  $\text{H}_2\text{O}$  was supplied to the anode at  $5 \text{ ml H}_2\text{O min}^{-1}$ , and dry  $\text{H}_2$  was supplied to the cathode at  $50 \text{ ml min}^{-1}$ . b) Voltammetric charge,  $q^*$ , obtained from integration of the absolute values of the currents of the CVs as a function of anode iridium loading. MEAs with low cathode loadings ( $\approx 0.025 \text{ mg}_{\text{Pt}} \text{ cm}^{-2}$ ) are represented by circles, MEAs with high cathode loadings ( $\approx 0.30 \text{ mg}_{\text{Pt}} \text{ cm}^{-2}$ ) are shown by triangles.

iii) Ir-specific power densities of  $\approx 0.01 \text{ g}_{\text{Ir}} \text{ kW}^{-1}$  to meet the iridium supply constraints for large-scale implementation. This means that the iridium loadings must be minimized while maintaining high current density at low electrolyzer cell voltages, whereby it is unclear whether this requirement can be met with the OER activity of currently known  $\text{IrO}_2$ -based anode catalysts.

The Ir-specific power density vs. current density shown in Fig. 10b is obtained from the measured polarization curves (cf. Fig. 10a) by dividing the anode Ir loading by the product of cell voltage and current density. The current density and Ir-specific power density at which the cell voltage efficiency corresponds to  $70\%_{\text{LHV}}$  ( $\equiv 1.79 \text{ V}$ ) is marked in Fig. 10b by the intersection of the dashed black line with the line representing each of the measured anode loadings (cathode Pt loadings are either  $0.30$  or  $0.025 \text{ mg}_{\text{Pt}} \text{ cm}^{-2}$ ). For conventionally used Ir loadings of  $\approx 1.6 \text{ mg}_{\text{Ir}} \text{ cm}^{-2}$  (blue and red lines in Fig. 10), the cell voltage efficiency target of  $70\%_{\text{LHV}}$  ( $\equiv 1.79 \text{ V}$ ) is met at a current density of  $\approx 3.6 \text{ A cm}^{-2}$  and an Ir-specific power density of  $\approx 0.25 \text{ g}_{\text{Ir}} \text{ kW}^{-1}$ . Quite clearly, this is still more than an order of magnitude higher than the target value of  $0.01 \text{ g}_{\text{Ir}} \text{ kW}^{-1}$  that we consider necessary for a large-scale decarbonization of the transportation sector by means of electrolytic hydrogen, even though ohmic losses were already minimized by using a thin membrane ( $\approx 50 \mu\text{m}$ ). Obviously, a significant

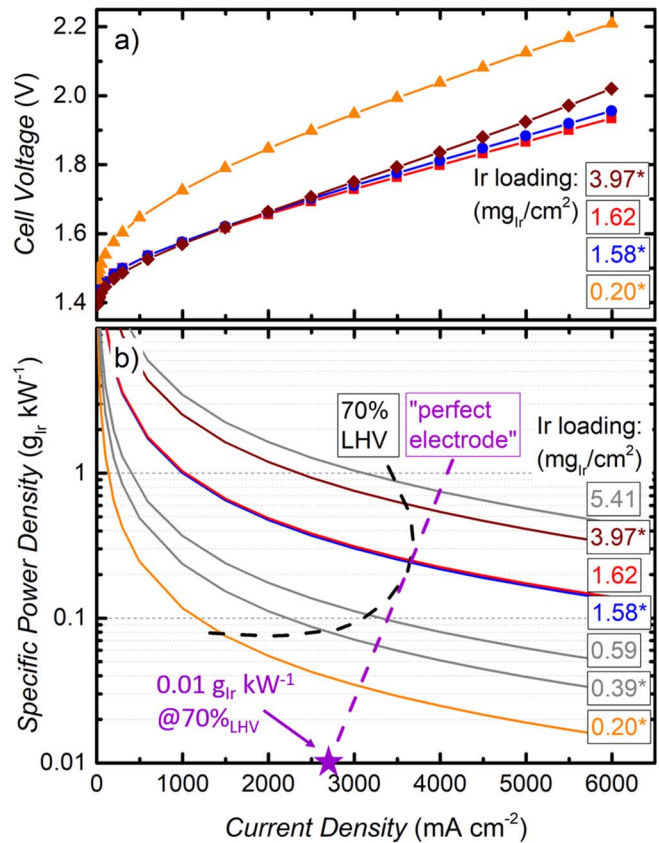


**Figure 10.** a) Ambient pressure polarization curves for different Ir anode loadings at  $80^\circ\text{C}$  ( $5 \text{ ml H}_2\text{O min}^{-1}$ ) with cathode loadings of either  $\approx 0.30 \text{ mg}_{\text{Pt}} \text{ cm}^{-2}$  or  $\approx 0.025 \text{ mg}_{\text{Pt}} \text{ cm}^{-2}$  (curves with low cathode loadings are marked by an asterisk at the anode loading label). b) Ir-specific power density as a function of current density for MEAs with different Ir loadings ( $0.20 - 5.41 \text{ mg}_{\text{Ir}} \text{ cm}^{-2}$ ). The black dashed line indicates an electrolyzer efficiency of  $70\%_{\text{LHV}}$ , corresponding to a cell voltage of  $1.79 \text{ V}$ . The purple dashed line indicates an electrolyzer efficiency of  $70\%_{\text{LHV}}$  based on the performance of the MEAs with standard Ir loadings ( $\approx 1.6 \text{ mg}_{\text{Ir}} \text{ cm}^{-2}$ ) and assuming that only the overpotential of the OER changes with Ir loading (Tafel slope:  $\approx 47 \text{ mV dec}^{-1}$ ), i.e., that HFR, proton and mass transport are similar for all MEAs and no additional losses occur for lower or higher Ir loadings. The purple star marks the target value of  $0.01 \text{ g}_{\text{Ir}} \text{ kW}^{-1}$  at an efficiency of  $70\%_{\text{LHV}}$ .

reduction of the Ir anode loading is required to reach the ambitious targets outlined above. If requiring a cell voltage efficiency of  $70\%_{\text{LHV}}$ , the minimum Ir-specific power density that can be reached with MEAs prepared in this work is  $\approx 0.08 \text{ g}_{\text{Ir}} \text{ kW}^{-1}$ , which was obtained for the lowest loaded anode with  $0.2 \text{ mg}_{\text{Ir}} \text{ cm}^{-2}$  (marked by the intersection of the orange line with the dashed black line in Fig. 10b) at a rather low current density of  $\approx 1.5 \text{ A cm}^{-2}$ .

Even though the lowest achieved Ir-specific power density is still 8-fold above the desired target, the poor performance of the low-loaded anode is not due to insufficient OER kinetics, but, as discussed above, caused by the inability to prepare such thin anode catalyst layers that are homogenous and contiguous, at least with the anode catalyst used in this study. While we have not been able to overcome this difficulty, one can still conduct a thought-experiment of how an  $\text{IrO}_2$ -based catalyst would perform at low loadings, if one were able to make a “perfect” homogenous and contiguous electrode that would have equally low transport resistances and HFR-values, as are observed for anodes with an optimal thickness between  $\approx 4 - 8 \mu\text{m}$  (here corresponding to a loading of  $1 - 2 \text{ mg}_{\text{Ir}} \text{ cm}^{-2}$ ; see Fig. 3). This thought-experiment can be conducted in the following manner based on the polarization curve with anode and cathode loadings of

1.58 mg<sub>Ir</sub> cm<sup>-2</sup> and 0.025 mg<sub>Pt</sub> cm<sup>-2</sup>, respectively (blue line in Fig. 10a): i) calculating the difference in OER overpotential for lower Ir loadings by means of Eq. 3 using a Tafel slope of 47 mV dec<sup>-1</sup>; ii) upshifting the polarization curve obtained for the MEA with the 1.58/0.025 mg<sub>PGM</sub> cm<sup>-2</sup> (anode/cathode) loading by the calculated OER overpotential difference; iii) determining the current density of the upshifted curve at a cell voltage of 1.79 V ( $\equiv 70\%_{LHV}$ ); and iv) dividing the assumed Ir loading by the resulting power density at 1.79 V and plotting the thus calculated Ir-specific power density vs. current density for different hypothetical Ir loadings. The thus projected Ir-specific power density vs. current density relationship for a “perfect” electrode at a cell voltage of 1.79 V is shown by the dashed purple line in Fig. 10b. It is based on the assumption that the HFR, as well as proton- and mass transport losses for the  $\approx 7\ \mu\text{m}$  thick standard MEA (with 1.58 mg<sub>Ir</sub> cm<sup>-2</sup> and 0.025 mg<sub>Pt</sub> cm<sup>-2</sup>) can be maintained constant independent of the Ir anode catalyst loading, i.e., that the Ir loading only affects the kinetic OER overpotential (cf. Eq. 3).

The “perfect” electrode projection (purple line in Fig. 10b) reveals that a Ir-specific power density of 0.01 g<sub>Ir</sub> kW<sup>-1</sup> at 1.79 V could be reached with an IrO<sub>2</sub>-based anode catalyst at a current density of  $\approx 2.7\ \text{A cm}^{-2}$  (x-axis intercept of the purple dashed line in Fig. 10b), i.e., at a power density of  $\approx 5\ \text{W cm}^{-2}$ . This, in turn, means that a catalyst with the same OER kinetics as the IrO<sub>2</sub>/TiO<sub>2</sub> catalyst used here, incorporated at a loading of  $\approx 0.05\ \text{mg}_{\text{Ir}}\ \text{cm}^{-2}$  (the product of 0.01 g<sub>Ir</sub> kW<sup>-1</sup> and  $\approx 5\ \text{W cm}^{-2}$ ) into a “perfect” electrode, would in principle be able to meet the target of 0.01 g<sub>Ir</sub> kW<sup>-1</sup> at 1.79 V. “Perfect” electrode in this context implies a homogeneous and contiguous electrode, which would not be possible for the IrO<sub>2</sub>/TiO<sub>2</sub> catalyst used in this work, because the corresponding anode thickness of  $\approx 0.2\ \mu\text{m}$  (based on its here measured packing density of  $4.3 \pm 0.3\ \mu\text{m}\ (\text{mg}_{\text{Ir}}\ \text{cm}^{-2})^{-1}$ ) could not be realized. The ideal thickness for a  $\approx 0.05\ \text{mg}_{\text{Ir}}\ \text{cm}^{-2}$  anode would rather be on the order of  $\approx 4\text{--}8\ \mu\text{m}$  (based on Fig. 3), which translates into an extremely low packing density of  $\approx 80\text{--}160\ \mu\text{m}\ (\text{mg}_{\text{Ir}}\ \text{cm}^{-2})^{-1}$ .

In fuel cell electrodes, such low packing densities are commonly used and are realized by supporting Pt nanoparticles on a highly structured carbon support; e.g., the packing density of a 15 wt% Pt/Vulcan catalyst is  $\approx 125\ \mu\text{m}\ (\text{mg}_{\text{Pt}}\ \text{cm}^{-2})^{-1}$  (based on  $22\ \mu\text{m}\ (\text{mg}_{\text{C}}\ \text{cm}^{-2})^{-1} \cdot (15/85\ \text{mg}_{\text{Pt}} \cdot \text{mg}_{\text{C}}^{-1})^{-1}$ ).<sup>17</sup> For an OER catalyst, however, this would require the deposition of Ir nanoparticles on a similarly high-structured support with sufficient electronic conductivity and stability at the high anodic potentials of an electrolyzer anode (precluding the use of carbon). Examples for this might include Ir nanoparticles deposited on, e.g., antimony-doped tin oxide (ATO).<sup>33,34</sup> In the absence of a suitable conductive oxide support, IrO<sub>2</sub> catalyst structures with a porosity of  $\approx 99\%$  (corresponding to  $\approx 85\ \mu\text{m}\ (\text{mg}_{\text{Ir}}\ \text{cm}^{-2})^{-1}$ ) would be required.

In summary, this illustrates that a large-scale application of PEM electrolysis is in principle feasible with Ir based catalysts. However, advanced catalyst concepts, viz., Ir or IrO<sub>2</sub> nanoparticles on conductive and oxidatively stable supports or Ir/IrO<sub>2</sub> aerogels with extremely high void volume would be necessary to fabricate homogeneous and contiguous catalyst layers at Ir loadings of  $\approx 0.05\ \text{mg}_{\text{Ir}}\ \text{cm}^{-2}$ . Concerning the Pt cathode catalyst, loadings of  $0.025\ \text{mg}_{\text{Pt}}\ \text{cm}^{-2}$  are possible without significant performance loss, which at a power density of  $\approx 5\ \text{W cm}^{-2}$  equates to only  $0.005\ \text{g}_{\text{Pt}}\ \text{kW}^{-1}$ . Assuming an annual installation capacity of  $\approx 150\ \text{GW}$  (cf. Introduction section), this translates into a Pt consumption of less than 1 ton/year, which should not be limiting considering the  $\approx 50$ -fold higher mining rate of Pt compared to Ir. While this analysis is based on the beginning-of-life performance of electrolyzer MEAs, it must be noted that it is still an open question as to whether sufficient durability can be obtained with such low catalyst loadings.

Finally, it needs to be stressed that our projections above present an extreme example based on the assumption that hydrogen were to solely replace fossil fuels in the transportation sector and that all hydrogen would be produced by PEM electrolysis. In reality, other technologies (e.g. battery electric vehicles) will also take a significant share of

vehicle propulsion systems in the future. Furthermore, alkaline electrolysis is a well-established technology and will likely continue to play an important role in electrolytic hydrogen production.<sup>35</sup> After all, while the final application might not actually require a specific power density as low as 0.01 g<sub>Ir</sub> kW<sup>-1</sup>, our work revealed that this ambitious target could be met with Ir-based catalysts if incorporated in an appropriate electrode structure.

## Conclusions

In this study, we presented an analysis of the influence of catalyst loading on the performance of a PEM electrolyzer using commercial Pt/C catalysts for the hydrogen evolution reaction (HER) and IrO<sub>2</sub>/TiO<sub>2</sub> for the oxygen evolution reaction (OER) in in-house prepared membrane electrode assemblies (MEAs) based on a 50  $\mu\text{m}$  Nafion 212 membrane. We showed that the Pt loading on the cathode has only a minor effect on the performance due to its high HER activity and that a reduction from  $0.30\ \text{mg}_{\text{Pt}}\ \text{cm}^{-2}$  to  $0.025\ \text{mg}_{\text{Pt}}\ \text{cm}^{-2}$  is possible without significant performance losses.

The Ir loading giving the best overall performance was found to be  $\approx 1\text{--}2\ \text{mg}_{\text{Ir}}\ \text{cm}^{-2}$ , which corresponds to an anode electrode thickness of  $\approx 4\text{--}8\ \mu\text{m}$ . For thicker electrodes ( $>10\ \mu\text{m}$ , Ir loading  $>2\ \text{mg}_{\text{Ir}}\ \text{cm}^{-2}$ ), an increase of cell voltage and HFR at high current densities was observed, which we attribute to the high water transport resistance through a thick catalyst layer, leading to a low water content in the membrane near the membrane/anode interface and an associated drop in membrane conductivity. On the other hand, for very thin anode electrodes ( $<2\ \mu\text{m}$ , Ir loading  $<0.5\ \text{mg}_{\text{Ir}}\ \text{cm}^{-2}$ ), the electrolyzer performance decreases drastically due to the inhomogeneous non-contiguous character of such thin catalyst layers, resulting in poor anode catalyst utilization and an associated higher HFR value. We have demonstrated that this effect can be mitigated by incorporating a porous transport layer (PTL) modified with a microporous layer.

Finally, we have evaluated the performance at various Ir loadings in the context of Ir-specific power requirements for large-scale applications, which we argue to be at or below  $\approx 0.01\ \text{g}_{\text{Ir}}\ \text{kW}^{-1}$  at  $70\%_{LHV}$  ( $\equiv 1.79\ \text{V}$  cell voltage). With the commercial IrO<sub>2</sub>/TiO<sub>2</sub> anode catalyst used in this study, it is not possible to reach this target value due to performance losses at low catalyst loadings or, more precisely, for thin electrodes. However, our analysis shows that the intrinsic OER activity of Ir-based catalysts would be sufficient to reach  $\approx 0.01\ \text{g}_{\text{Ir}}\ \text{kW}^{-1}$  at 1.79 V, if the packing density of iridium in the electrode can be reduced, so that  $\approx 4\text{--}8\ \mu\text{m}$  thick electrodes with an Ir loading of only  $\approx 0.05\ \text{mg}_{\text{Ir}}\ \text{cm}^{-2}$  can be made. This shows that catalyst morphology/structure may be equally important as its OER activity.

## Acknowledgments

This work was funded by the Bavarian Ministry of Economic Affairs and Media, Energy and Technology through the project ZAE-ST (storage technologies) as well as by the German Federal Ministry of Education and Research (BMBF) in the framework of the Kopernikus P2X project (funding number 03SFK2V0). We thank Matthias Singer for electrode preparation as well as Alexandra Weiß and Maximilian Möckl for reviewing the paper. The electron microscopy was accomplished at the WACKER-Chair of Molecular Chemistry of the TUM with the assistance of Katia Rodewald.

## Appendix

The expected kinetic overpotential for the hydrogen evolution reaction (HER),  $\eta_{\text{HER}}$ , for the different Pt loadings can be estimated via linearization of the Butler-Volmer equation:<sup>36,37</sup>

$$\eta_{\text{HER}} = i \cdot R_{\text{K,HER}} \quad [\text{A1}]$$

where

$$R_{\text{K,HER}} = \frac{RT}{(\alpha_a + \alpha_c) \cdot F \cdot L_{\text{Pt}} \cdot A_{\text{Pt,el}} \cdot i_0, \text{HER}} \quad [\text{A2}]$$

With an HER exchange current density of  $i_{0,\text{HER}} = 250 \text{ mA cm}^{-2,\text{metal}}$  (for  $\alpha_a + \alpha_c = 1$ ) at  $80^\circ\text{C}$ ,<sup>7,8</sup> cathode catalyst loading of  $L_{\text{Pt}}(45.8\text{wt\% Pt}) = 0.30 \text{ mg}_{\text{Pt}}/\text{cm}^2$  or  $L_{\text{Pt}}(4.8\text{wt\% Pt}) = 0.025 \text{ mg}_{\text{Pt}}/\text{cm}^2$ , and electrochemically active surface area of  $A_{\text{Pt,el}}(45.8\text{wt\% Pt}) = 60 \text{ m}^2/\text{g}_{\text{pt}}$ <sup>37</sup> or  $A_{\text{Pt,el}}(4.8\text{wt\% Pt}) = 110 \text{ m}^2/\text{g}_{\text{pt}}$ ,<sup>7,8</sup>  $R_{\text{K,HER}}$  amounts to  $\approx 0.7 \text{ m}\Omega \text{ cm}^2$  for the high Pt loading and  $\approx 4.4 \text{ m}\Omega \text{ cm}^2$  for the low Pt loading. This results in a difference  $\Delta R_{\text{K,HER}} = 3.7 \text{ m}\Omega \text{ cm}^2$ .

The effective proton transport resistance for the hydrogen cathode can be calculated following the approach described by Gu et al.<sup>37</sup>

$$\frac{R_{\text{H}^+, \text{cath}}^{\text{eff}}}{R_{\text{H}^+, \text{cath}}} = \frac{1}{\beta} \cdot \left( \frac{e^\beta + e^{-\beta}}{e^\beta - e^{-\beta}} - \frac{1}{\beta} \right) \quad [\text{A3}]$$

where

$$\beta = \left( \frac{R_{\text{H}^+, \text{cath}}}{R_{\text{K,HER}}} \right)^{1/2} \quad [\text{A4}]$$

Here, the sheet resistance for proton transport in a Pt/C electrode,  $R_{\text{H}^+, \text{cath}}$ , can be calculated from the reported sheet resistivity of  $\approx 25 \Omega \text{ cm}$  for a Pt/Vulcan electrode with an I/C-ratio of 0.6/1 at  $80^\circ\text{C}$  and a relative humidity of 122 % (i.e., in the presence of liquid water)<sup>38</sup> and the electrode thicknesses of  $\approx 8 \mu\text{m}$  for the high-loaded and  $\approx 11 \mu\text{m}$  for low-loaded cathode (s. Experimental Section), equating to proton conduction sheet resistances of  $R_{\text{H}^+, \text{cath}}(45.8\text{wt\% Pt}) \approx 20 \text{ m}\Omega \text{ cm}^2$  and  $R_{\text{H}^+, \text{cath}}(4.8\text{wt\% Pt}) \approx 27.5 \text{ m}\Omega \text{ cm}^2$ . Together with the above determined charge transfer resistances ( $R_{\text{K,HER}}(45.8\text{wt\% Pt}) \approx 0.7 \text{ m}\Omega \text{ cm}^2$  and  $R_{\text{K,HER}}(4.8\text{wt\% Pt}) \approx 4.4 \text{ m}\Omega \text{ cm}^2$ ), this yields  $\beta$ -values of  $\approx 5.4$  for the high-loaded and  $\approx 2.5$  for the low-loaded cathode (s. Eq. A4). Thus, the effective proton transport resistance,  $R_{\text{H}^+, \text{cath}}^{\text{eff}}$ , calculated by Eq. A3 is  $\approx 3 \text{ m}\Omega \text{ cm}^2$  for the high-loaded and  $\approx 6.8 \text{ m}\Omega \text{ cm}^2$  for the low-loaded cathode. From the sum of kinetic and proton transport resistance ( $R_{\text{K,HER}} + R_{\text{H}^+, \text{cath}}^{\text{eff}}(45.8\text{wt\% Pt}) \approx 3.7 \text{ m}\Omega \text{ cm}^2$  and  $R_{\text{K,HER}} + R_{\text{H}^+, \text{cath}}^{\text{eff}}(4.8\text{wt\% Pt}) \approx 11.2 \text{ m}\Omega \text{ cm}^2$ ) one can calculate a total difference of  $\approx 7.5 \text{ m}\Omega \text{ cm}^2$  between high-loaded and low-loaded cathode.

## ORCID

Maximilian Bernt  <https://orcid.org/0000-0001-8448-5532>  
Armin Siebel  <https://orcid.org/0000-0001-5773-3342>

## References

1. L. Bertuccioli, A. Chan, D. Hart, F. Lehner, B. Madden, and E. Standen, Study on Development of Water Electrolysis in the EU, in *Fuel Cells and Hydrogen Joint Undertaking* (2014).
2. T. Smolinka, M. Günther, and J. Garche, Stand und Entwicklungspotenzial der Wasserelektrolyse zur Herstellung von Wasserstoff aus regenerativen Energien, in *Kurzfassung des Abschlussberichtes NOW-Studie* (2011).
3. K. E. Ayers, J. N. Renner, N. Danilovic, J. X. Wang, Y. Zhang, R. Maric, and H. Yu, *Catalysis Today*, **262**, 121 (2016).
4. U. Babic, M. Suermann, F. N. Büchi, L. Gubler, and T. J. Schmidt, *Journal of The Electrochemical Society*, **164**, F387 (2017).
5. K. E. Ayers, E. B. Anderson, C. Capuano, B. Carter, L. Dalton, G. Hanlon, J. Manco, and M. Niedzwiecki, *ECS Transactions*, **33**, 3 (2010).
6. M. Carmo, D. L. Fritz, J. Mergel, and D. Stolten, *International Journal of Hydrogen Energy*, **38**, 4901 (2013).
7. J. Durst, A. Siebel, C. Simon, F. Hasché, J. Herranz, and H. A. Gasteiger, *Energy Environ. Sci.*, **7**, 2255 (2014).
8. J. Durst, C. Simon, F. Hasché, and H. A. Gasteiger, *Journal of the Electrochemical Society*, **162**, F190 (2015).
9. IEA, *Key World Energy Statistics 2016* (2017).
10. C. K. Mittelstaedt, *ECS Trans.*, **69**, 205 (2015).
11. L. Ma, S. Sui, and Y. Zhai, *International Journal of Hydrogen Energy*, **34**, 678 (2009).
12. J. Polonský, P. Mazúr, M. Paidar, E. Christensen, and K. Bouzek, *International Journal of Hydrogen Energy*, **39**, 3072 (2014).
13. P. Mazúr, J. Polonský, M. Paidar, and K. Bouzek, *International Journal of Hydrogen Energy*, **37**, 12081 (2012).
14. K. A. Lewinski, D. F. v. d. Vliet, and S. M. Luopa, *ECS Transactions*, **69**, 893 (2015).
15. C. Rozain, E. Mayousse, N. Guillet, and P. Millet, *Applied Catalysis B: Environmental*, **182**, 153 (2016).
16. C. Rozain, E. Mayousse, N. Guillet, and P. Millet, *Applied Catalysis B: Environmental*, **182**, 123 (2016).
17. G. S. Harzer, J. N. Schwämmlein, A. M. Damjanović, S. Ghosh, and H. A. Gasteiger, *Journal of The Electrochemical Society*, **165**, F3118 (2018).
18. M. Bernt and H. A. Gasteiger, *Journal of The Electrochemical Society*, **163**, F3179 (2016).
19. P. J. Rheinländer, M. Bernt, Y. Incedag, and H. A. Gasteiger, *Meeting Abstracts*, **MA2016-02**, 2427 (2016).
20. M. Suermann, T. J. Schmidt, and F. N. Büchi, *ECS Transactions*, **69**, 1141 (2015).
21. T. E. Springer, T. Zawodzinski, and S. Gottesfeld, *Journal of the Electrochemical Society*, **138**, 2334 (1991).
22. S. Gottesfeld and T. A. Zawodzinski, in *Advances in Electrochemical Science and Engineering*, R. C. Alkire, H. Gerischer, D. M. Kolb and C. W. Tobias Editors, John Wiley & Sons (1997).
23. M. Doyle and G. Rajendran, in *Handbook of Fuel Cells: Fundamentals, Technology, and Applications*, W. Vielstich, A. Lamm, and H. A. Gasteiger Editors, p. 18, John Wiley & Sons, New York (2003).
24. M. Suermann, A. Pätru, T. J. Schmidt, and F. N. Büchi, *International Journal of Hydrogen Energy*, **42**, 12076 (2017).
25. S. A. Grigoriev, P. Millet, S. V. Korobtsev, V. I. Poremskiy, M. Pepic, C. Etievant, C. Puyenchet, and V. N. Fateev, *International Journal of Hydrogen Energy*, **34**, 5986 (2009).
26. M. Suermann, T. J. Schmidt, and F. N. Büchi, *Electrochimica Acta*, **211**, 989 (2016).
27. M. Suermann, K. Takahashi, A. Lambrac, T. J. Schmidt, and F. N. Büchi, *Journal of The Electrochemical Society*, **164**, F973 (2017).
28. Y. Matsumoto and E. Sato, *Materials Chemistry and Physics*, **14**, 397 (1986).
29. T. Reier, D. Teschner, T. Lunkenbein, A. Bergmann, S. Selve, R. Krahnert, R. Schlogl, and P. Strasser, *Journal of The Electrochemical Society*, **161**, F876 (2014).
30. G. Lodi, E. Sivieri, A. De Battisti, and S. Trasatti, *Journal of Applied Electrochemistry*, **8**, 135 (1978).
31. S. Ardzizzone, G. Fregonara, and S. Trasatti, *Electrochimica Acta*, **35**, 263 (1990).
32. P. Lettenmeier, S. Kolb, F. Burggraf, A. S. Gago, and K. A. Friedrich, *Journal of Power Sources*, **311**, 153 (2016).
33. H.-S. Oh, H. N. Nong, T. Reier, M. Gliech, and P. Strasser, *Chemical Science*, **6**, 3321 (2015).
34. G. Liu, J. Xu, Y. Wang, and X. Wang, *Journal of Materials Chemistry A*, **3**, 20791 (2015).
35. A. Buttler and H. Spiethoff, *Renewable and Sustainable Energy Reviews*, **82**, 2440 (2018).
36. K. C. Neyerlin, W. Gu, J. Jorne, and H. A. Gasteiger, *Journal of The Electrochemical Society*, **154**, B631 (2007).
37. W. Gu, D. R. Baker, Y. Liu, and H. A. Gasteiger, in *Handbook of Fuel Cells*, W. Vielstich, H. A. Gasteiger, and H. Yokokama Editors, p. 631, John Wiley & Sons, Chichester, UK (2009).
38. Y. Liu, M. W. Murphy, D. R. Baker, W. Gu, C. Ji, J. Jorne, and H. A. Gasteiger, *Journal of The Electrochemical Society*, **156**, B970 (2009).